

## Evidence for Resonance Scattering in the X-ray Grating Spectrum of the Supernova Remnant N49

YUKI AMANO,<sup>1</sup> HIROYUKI UCHIDA,<sup>1</sup> TAKA AKI TANAKA,<sup>1</sup> LIYI GU,<sup>2,3</sup> AND TAKESHI GO TSURU<sup>1</sup>

<sup>1</sup>*Department of Physics, Kyoto University, Kitashirakawa Oiwake-cho, Sakyo, Kyoto, Kyoto 606-8502, Japan*

<sup>2</sup>*RIKEN High Energy Astrophysics Laboratory, 2-1 Hirosawa, Wako, Saitama 351-0198, Japan*

<sup>3</sup>*SRON Netherlands Institute for Space Research, Sorbonnelaan 2, 3584 CA Utrecht, the Netherlands*

(Received January 1, 2018; Revised January 7, 2018; Accepted May 12, 2020)

### ABSTRACT

Resonance scattering (RS) is an important process in astronomical objects, because it affects measurements of elemental abundances and distorts surface brightness of the object. It is predicted that RS can occur in plasmas of supernova remnants (SNRs). Although several authors reported hints of RS in SNRs, no strong observational evidence has been established so far. We perform a high-resolution X-ray spectroscopy of the SNR N49 with the Reflection Grating Spectrometer aboard XMM-Newton. The RGS spectrum of N49 shows a high G-ratio of O VII He $\alpha$  lines as well as O VIII Ly $\beta$ / $\alpha$  and Fe XVII (3s–2p)/(3d–2p) ratios which cannot be explained by the emission from a thin thermal plasma. These line ratios can be well explained by the effect of RS. Our result implies that RS has a large impact particularly on a measurement of the oxygen abundance.

*Keywords:* ISM: supernova remnants — scattering — opacity — X-rays: ISM — Individual: N49

### 1. INTRODUCTION

X-ray imaging spectroscopy of astronomical objects provides us with many insights into their chemical evolution and formation mechanism. This is partially because X-ray emitting plasmas are often optically thin, which allows us to directly estimate its elemental abundances and their spatial distributions. However, resonance lines such as O VII He $\alpha$  and Fe XVII L $\alpha$  may suffer from effects of scattering (resonance scattering: RS), as discussed in the cases of galaxies (e.g., Xu et al. 2002), solar active regions (e.g., Rugge & McKenzie 1985), and galaxy clusters (e.g., Hitomi Collaboration 2018).

RS is an apparent scattering phenomenon due to an absorption and re-emission of line photons by ions. Since the RS effect apparently reduces intensities of some lines and/or distorts profiles of surface brightness (Shigeyama 1998), ignoring its contribution can sometimes lead to, for example, biases in elemental abundance measurements. On the other hand, if RS is significant, quantifying its contribution will allow us to measure several important parameters such as micro-turbulence ve-

locities (de Plaa et al. 2012) and absolute abundances (Waljeski et al. 1994).

Kaastra & Mewe (1995) predicted that RS of X-ray photons can occur in a plasma with a large depth along the line of sight such as a rim of supernova remnants (SNRs). Several observational signatures of RS have been reported such as a high forbidden-to-resonance ratio of O VII He $\alpha$  obtained from grating spectra of DEM L71 (van der Heyden et al. 2003) and N23 (Broersen et al. 2011). A difference in surface brightness between forbidden and resonance lines also supports the presence of RS (e.g., van der Heyden et al. 2003). Based on a Suzaku observation of the Cygnus Loop, Miyata et al. (2008) claimed that a depleted abundance of O may be partially explained by RS. A recent grating observation of the Loop also hints at a possibility of RS (Uchida et al. 2019). These studies suggest that the RS effect may potentially be significant in SNRs. However, no strong observational evidence has been established so far.

N49 is a middle-aged ( $\sim 4800$  yr; Park et al. 2012) SNR located in the Large Magellanic Cloud (LMC). Although the origin of N49 is somewhat controversial, most of recent researches support that it originated from a core-collapse explosion based on a possible association with the soft gamma-ray repeater

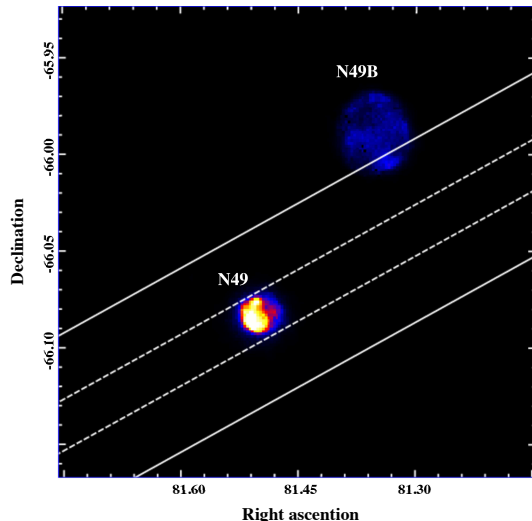


**Figure 1.** EPIC-MOS image (0.4–8.0 keV) of N49. The cross-dispersion width of the RGS (5 arcmin) is in between the white solid line. The spectral extraction region is enclosed by the white dashed line. N49B is another SNR near N49.

(SGR) 0526–66 (Cline et al. 1982) and the presence of a dense interstellar medium (ISM) (e.g., Banas et al. 1997; Yamaguchi et al. 2014). The thermal X-ray emission is explained by a mixture of two components; metal-rich ejecta and a shock-heated ISM (Park et al. 2003, 2012; Uchida et al. 2015). It is also notable that N49 is in an overionized state (Uchida et al. 2015) and is interacting with dense molecular clouds on the eastern side (Banas et al. 1997; Yamane et al. 2018). Due to the interaction with molecular clouds, the thermal X-ray emission of N49 is particularly bright on the southeastern rim. N49 is an attractive object since Kaastra & Mewe (1995) pointed out that the effect of RS can show up if an SNR has such a spherically asymmetric structure.

Here, we present a high-resolution X-ray spectroscopy of N49 with the Reflection Grating Spectrometer (RGS) aboard XMM-Newton. The obtained G-ratio of O VII He $\alpha$  and other line ratios as well imply a non-negligible contribution of RS in N49. Throughout the paper, errors are given at a 68% confidence level. We assume the distance to N49 (LMC) to be 50 kpc (Pietrzyński et al. 2013).

## 2. OBSERVATION AND DATA REDUCTION

N49 was observed with the XMM-Newton satellite (Jansen et al. 2001) in 2001 (Obs.ID 0113000201) and 2007 (Obs.ID 0505310101). The observation in 2007 was performed with a roll angle which placed N49 and a nearby SNR, N49B, along the dispersion direction of the RGS, making it difficult to extract RGS

spectra of N49. We thus analyzed only the data obtained in 2001. For our spectral analysis, we used the RGS (den Herder et al. 2001) and the European Photon Imaging Camera MOS (Turner et al. 2001) data. We reduced the data using XMM Science Analysis Software version 16.1.0. The RGS data were processed with the RGS pipeline tool `rgsproc`. To discard periods of background flares, we applied good time intervals based on the count rate in CCD9, which is the closest to the optical axis of the mirror and has the least X-ray counts from the source, and most affected by the background flares. The resulting effective exposure time is 11 ks for both RGS1 and RGS2. Since the second order spectra are of low statistical quality, we analyzed only the first order spectra.

## 3. ANALYSIS

We analyzed the spectra using version 3.04.0 of the SRON SPEX package (Kaastra et al. 1996) with the maximum likelihood C-statistic (Cash 1979; Kaastra 2017). The RGS spectra were fitted simultaneously with those of MOS1 and 2. To account for the spatial broadening of the source, we multiplied spectral models with the SPEX model `lpro`, to which we input the MOS1 image of the source. Our models have two absorption models: one for the Milky Way and the other for the LMC. The column density of the former was fixed to  $6 \times 10^{20} \text{ cm}^{-2}$  (Dickey & Lockman 1990) whereas that of the latter is left free. The elemental abundances for the LMC absorption were fixed to values found in literature ( $\sim 0.3$  solar; Russell & Dopita 1992; Schenck et al. 2016).

Figure 2 shows MOS1 and combined RGS1+2 spectra of N49. Prominent lines are detected at  $\sim 12 \text{ \AA}$  (Ne X Ly $\alpha$ ),  $\sim 13.5 \text{ \AA}$  (Ne IX He $\alpha$ ),  $\sim 15 \text{ \AA}$  (Fe XVII L $\alpha$ ; 3d–2p),  $\sim 16 \text{ \AA}$  (O VIII Ly $\beta$ ),  $\sim 17 \text{ \AA}$  (Fe XVII L $\alpha$ ; 3s–2p),  $\sim 20 \text{ \AA}$  (O VII He $\beta$ , O VIII Ly $\alpha$ ),  $\sim 22 \text{ \AA}$  (O VII He $\alpha$ ). We applied a two-component nonequilibrium ionization (NEI) model (`nej`; Kaastra & Jansen 1993) absorbed by neutral gas to the spectra. The NEI model consists of emissions from the overionized hot ejecta and an ionizing cool component originating from the swept-up ISM (Uchida et al. 2015). Although SGR 0526–66 cannot be spatially resolved with the RGS, according to the result of Uchida et al. (2015), the emission is negligible compared to that from N49 in the energy band covered by the RGS (0.3–2.0 keV).

Free parameters of the NEI components include the electron temperature ( $kT_e$ ), ionization time scale ( $n_e t$ , where  $n_e$  and  $t$  are the electron number density and the elapsed time since shock heating or rapid cooling, respectively), and emission measure ( $n_e n_H V$ ). In addition

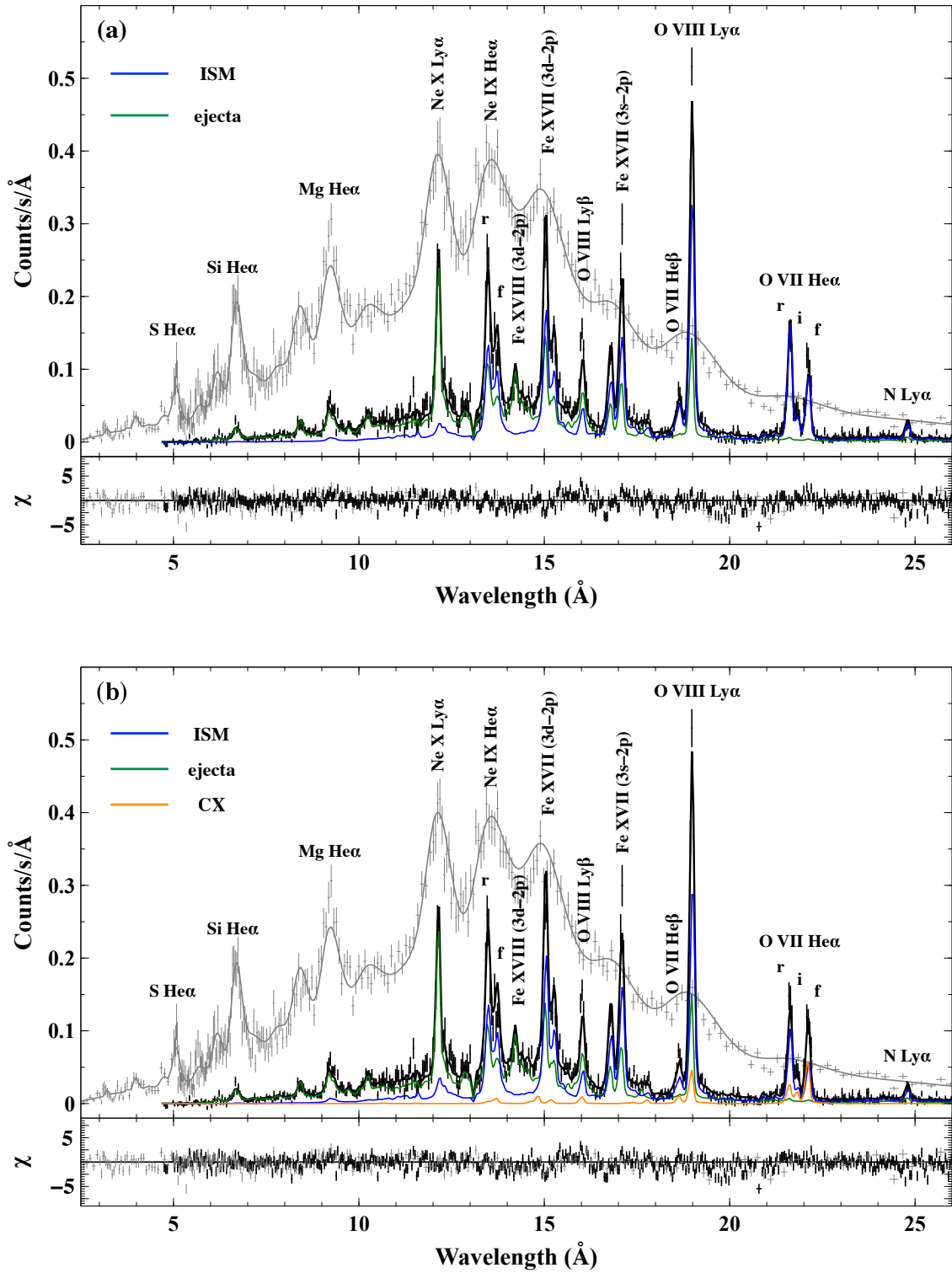


**Figure 2.** RGS1+2 (black) and MOS1 (gray) spectra of N49. Overlaid in panels (a) and (b) are the best-fit “NEI” and “NEI+CX” models, respectively.

**Table 1.** Best-fit parameters of the N49 spectrum

| Component                                      | Parameters (unit)  | NEI   | NEI + CX               | NEI - Gaussians (RS)                |                 |
|--|--|---|------------------------|-------------------------------------|-----------------|
| Absorption                                     | $N_{\text{H}}(\text{MW})$ ( $10^{22} \text{ cm}^{-2}$ )  | 0.6 (fixed)                                   | 0.6 (fixed)            | 0.6 (fixed)                         |                 |
|  | $N_{\text{H}}(\text{LMC})$ ( $10^{22} \text{ cm}^{-2}$ ) | $3.1 \pm 0.1$                                 | $2.8 \pm 0.1$          | $3.3 \pm 0.1$                       |                 |
| ISM  | $kT_{\text{e}}$ (keV)                                    | $0.204 \pm 0.003$                             | $0.230 \pm 0.006$      | $0.205 \pm 0.003$                   |                 |
|  | $n_{\text{e}}t$ ( $10^{11} \text{ cm}^{-3} \text{ s}$ )  | $> 10$  | $> 10$                 | $> 10$                              |                 |
|  | $EM$ ( $10^{56} \text{ cm}^{-3}$ )                       | $260 \pm 20$                                  | $170_{-10}^{+20}$      | $322_{-22}^{+23}$                   |                 |
| Ejecta   | $kT_{\text{e}}$ (keV)                                    | $0.61 \pm 0.01$                               | $0.63 \pm 0.01$        | $0.56_{-0.01}^{+0.08}$              |                 |
|  | $kT_{\text{init}}$ (keV)                                 | 11 (fixed)                                    | 11 (fixed)             | 11 (fixed)                          |                 |
|  | $n_{\text{e}}t$ ( $10^{11} \text{ cm}^{-3} \text{ s}$ )  | $7.2_{-0.3}^{+0.5}$                           | $7.2_{-0.3}^{+0.4}$    | $6.9_{-0.4}^{+1.0}$                 |                 |
|  | O (= C = N)  | $0.71_{0.06}^{+0.16}$                         | $0.67_{-0.14}^{+0.20}$ | $1.3 \pm 0.1$                       |                 |
|  | Ne   | $0.96_{-0.07}^{+0.09}$                        | $0.94_{-0.06}^{+0.09}$ | $1.0 \pm 0, 1$                      |                 |
|  | Mg   | $0.75 \pm 0.07$                               | $0.72_{-0.06}^{+0.07}$ | 0.75(fixed)                         |                 |
|  | Si   | $0.87_{-0.06}^{+0.08}$                        | $0.85_{-0.06}^{+0.08}$ | 0.87(fixed)                         |                 |
|  | S  | $1.2 \pm 0.1$                                 | $1.2 \pm 0.1$          | 1.2(fixed)                          |                 |
|  | Ar   | $1.8 \pm 0.5$                                 | $1.8_{-0.3}^{+0.4}$    | 1.8(fixed)                          |                 |
|  | Fe   | $0.32 \pm 0.03$                               | $0.29_{-0.02}^{+0.03}$ | $0.32 \pm 0.01$                     |                 |
|  | $EM$ ( $10^{56} \text{ cm}^{-3}$ )                       | $58 \pm 4$                                    | $57_{-2}^{+5}$         | $53 \pm 0.1$                        |                 |
|  | CX   | $kT_{\text{e}}$ (keV)                         | ...                    | (= value of the ISM component)      | ...             |
|  |  | abundance                                     | ...                    | (= abundances of the ISM component) | ...             |
| $v_{\text{collision}}$ ( $\text{km s}^{-1}$ )  |  | ...   | $270 \pm 110$          | ...                                 |                 |
| $EM$ ( $10^{56} \text{ cm}^{-3}$ )             |  | ...   | $47_{-13}^{+25}$       | ...                                 |                 |
| Gaussian: Ne IX He $\alpha$                    |  | Normalization ( $10^{44} \text{ ph s}^{-1}$ ) | ...                    | ...                                 | $0.36 \pm 0.09$ |
| Fe XVII L $\alpha$ ( $\sim 15.0 \text{ \AA}$ ) | ...  | ...   | ...                    | $0.92 \pm 0.11$                     |                 |
| Fe XVII L $\alpha$ ( $\sim 15.3 \text{ \AA}$ ) | ...  | ...   | ...                    | $< 6.9 \times 10^{-2}$              |                 |
| O VIII Ly $\beta$                              | ...  | ...   | ...                    | $< 1.3 \times 10^{-2}$              |                 |
| Fe XVII L $\alpha$ ( $\sim 16.8 \text{ \AA}$ ) | ...  | ...   | ...                    | $0.50 \pm 0.12$                     |                 |
| Fe XVII L $\alpha$ ( $\sim 17.1 \text{ \AA}$ ) | ...  | ...   | ...                    | $< 1.5 \times 10^{-3}$              |                 |
| O VII He $\beta$                               | ...  | ...   | ...                    | $< 5.8 \times 10^{-2}$              |                 |
| O VIII Ly $\alpha$                             | ...  | ...   | ...                    | $4.6 \pm 0.3$                       |                 |
| O VII He $\alpha$ (r)                          | ...  | ...   | ...                    | $2.5 \pm 0.5$                       |                 |
| O VII He $\alpha$ (i)                          | ...  | ...   | ...                    | $< 3.0 \times 10^{-3}$              |                 |
| C-statistic/d.o.f.                             |  | 4700/3211                                     | 4660/3214              | 4611/3190                           |                 |

NOTE—The elemental abundances are given with respect to the solar values by [Lodders et al. \(2009\)](#).

NOTE—See Table 2 for the line centroid wavelengths of the Gaussians.

to these parameters, the abundances of O ( $=N=C$ ), Ne, Mg, Si, S, Ar, and Fe ( $=Ni$ ) of the ejecta were set free. The `neij` model has another parameter  $kT_{\text{init}}$ , which represents an initial temperature before a rapid cooling or a shock heating of the plasma. Uchida et al. (2015) determined  $kT_{\text{init}}$  for the ejecta component mainly from the ionization state of the Fe  $K\alpha$  emission at  $\sim 6.6$  keV. Since the line centroid is out of the wavelength band of the RGS data, we fixed  $kT_{\text{init}}$  of the ejecta component at 11 keV based on Uchida et al. (2015). On the other hand, the  $kT_{\text{init}}$  of the ISM component is fixed at  $\sim 0$  keV.

Figure 2 (a) shows the result of the spectral fitting with the two-component NEI model (hereafter, NEI model). The best-fit parameters are listed in Table 1. The model well reproduces the overall MOS spectrum; the best-fit parameters of  $kT_e$  and  $n_e t$  of the ejecta component are consistent with those obtained by Uchida et al. (2015). Focusing on the RGS spectrum in Figure 3, however, we found discrepancies between the model and the data especially around the O VII triplet, O VIII  $\text{Ly}\beta$ , and Fe XVII  $\text{L}\alpha$  series.

We first focus on the O VII  $\text{He}\alpha$  line, more specifically on its G-ratio  $(F + I)/R$ , where  $F$ ,  $I$ , and  $R$  are intensities of the forbidden, intercombination, and resonance lines, respectively. The G-ratio of the O VII  $\text{He}\alpha$  line strongly depends on  $kT_e$  as presented in Figure 4. We assume here that the emitting plasma is in an ionizing state since most of the O VII  $\text{He}\alpha$  line emission of N49 is attributed to the shocked ISM (Figure 2 (a)). Fitting with four Gaussians, we estimated the G-ratio of the O VII  $\text{He}\alpha$  line observed in N49, which is plotted in Figure 4. The observed G-ratio obviously requires an unreasonably low  $kT_e$  ( $< 0.15$  keV) with any reasonable range of  $n_e t$ , indicating necessity of some physical process to enhance the G-ratio.

Charge exchange (CX) is one of the possible processes to make the G-ratio higher. Recent X-ray spectroscopy studies with gratings found enhanced  $F/R$  ratios of O VII in Puppis A (Katsuda et al. 2012), and the Cygnus Loop (Uchida et al. 2019). They claimed that the anomalous line ratios are explained by CX X-ray emission. As suggested by Uchida et al. (2019), the CX emission can be enhanced particularly in a region where a shock is interacting with dense gas. CX is therefore promising in the case of N49 since it is interacting with surrounding molecular clouds (Yamane et al. 2018). We thus added a CX model (Gu et al. 2016a) to the NEI model. All the abundances and  $kT_e$  for the CX component were coupled to those of the ISM component. The collision velocity  $v_{\text{collision}}$  (*i.e.* shock velocity) was allowed to vary. We assumed a multiple collision case

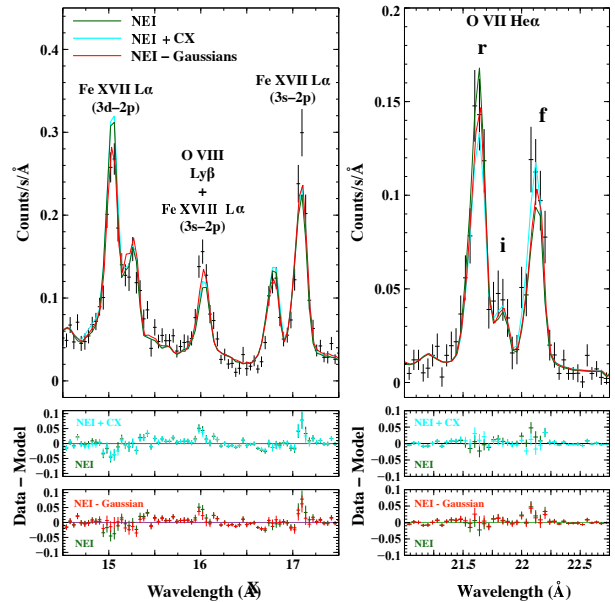


**Figure 3.** Close-up views of the RGS spectrum (Figure 2) around Fe XVII  $\text{L}\alpha$  and O VIII  $\text{Ly}\beta$  (left) and O VII  $\text{He}\alpha$  (right). The dark green, cyan, and red solid lines in the top panels represent the best-fit “NEI”, “NEI+CX”, and “NEI–Gaussians” models, respectively. The middle and bottom panels show residuals from the models with the same color scheme as the top panels.

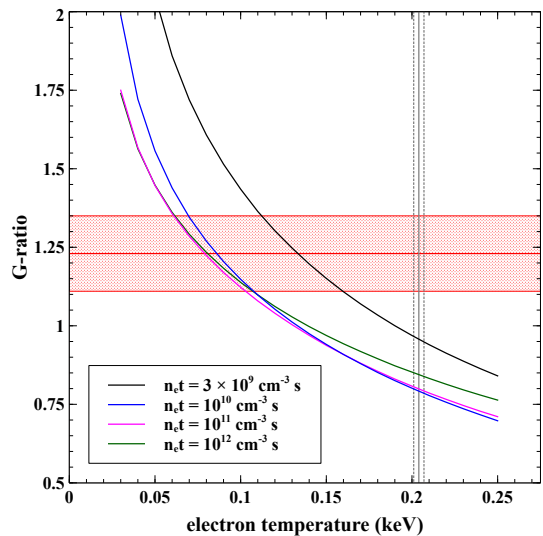


**Figure 4.** Relation between  $kT_e$  and the G-ratio of O VII  $\text{He}\alpha$ . The solid curves represent the G-ratio expected for an ionizing plasma emission predicted by the `neij` model in SPEX. The colors of each line indicate  $n_e t$  assumed. The red hatched area denotes the G-ratio derived from the observed line ratio and its statistical error. The gray lines indicates  $kT_e$  from the best-fit NEI model.

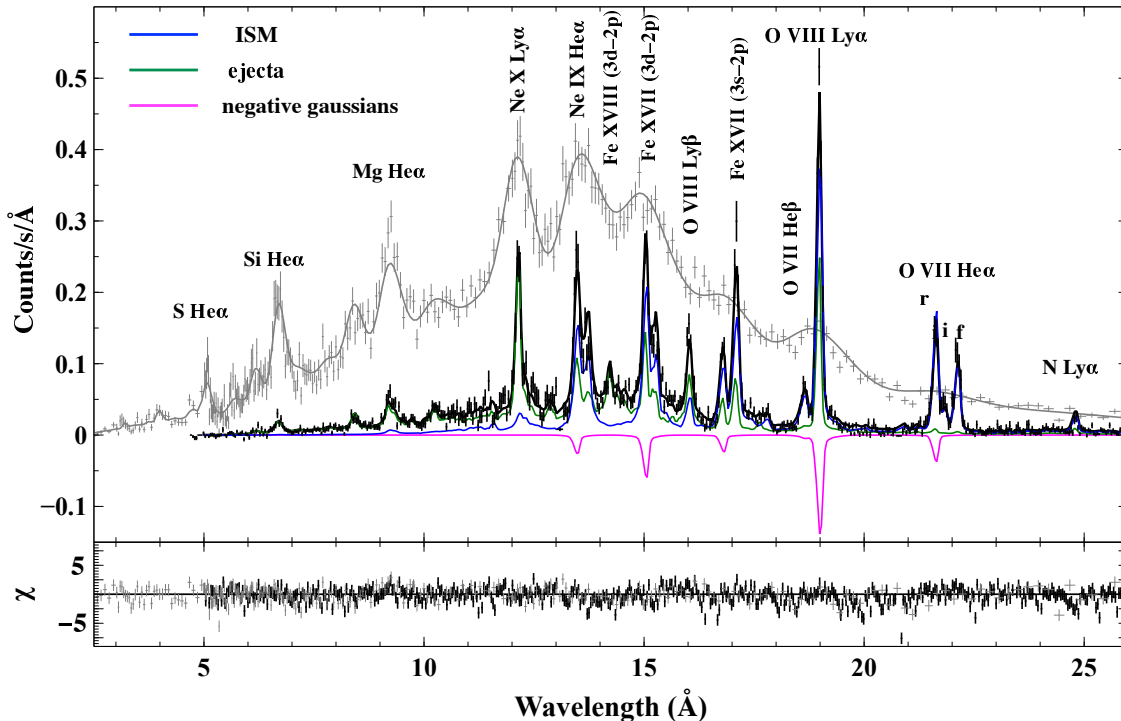


**Figure 5.** Same as Figure 2 but with the “NEI – Gaussians” model. The magenta solid line represents the negative Gaussians.

in which an ion continuously undergoes CX until it becomes neutral. The best-fit “NEI+CX” model is displayed in Figure 2 (b), and the parameters are listed in Table 1. Although the addition of the CX component improves the residuals at the O VII triplet, the discrepancies still remain around O VIII Ly $\beta$  and Fe XVII L $\alpha$  series (Figure 3). Therefore, we conclude that the NEI + CX model is insufficient to describe the spectrum of N49.

RS is another possible process that would be responsible for the enhanced G-ratio. If photons of the resonance line are scattered off the line of sight due to RS, observed  $R$  would become lower and the G-ratio would be enhanced. The observed high Fe XVII (3s-2p)/(3d-2p) and O VIII Ly $\beta$ / $\alpha$  ratios can also be caused by RS, as pointed out by previous studies (e.g., Xu et al. 2002; Hitomi Collaboration 2018). To quantify the contribution of the scattering effect, we added negative Gaussians at wavelengths where lines of the ISM component are prominent in the best-fit NEI model: the O VII He $\alpha$  intercombination, O VII He $\alpha$  resonance, O VII He $\beta$ , O VIII Ly $\alpha$ , O VIII Ly $\beta$ , Fe XVII L $\alpha$ , and Ne IX He $\alpha$  resonance lines. Since the oscillator strengths of the O VII and Ne IX forbidden lines are several orders of magnitude smaller than those of the other lines, we assume that the scattering effect is negligible for the forbidden lines. The free parameters of the NEI components are

the electron temperature ( $kT_e$ ), ionization time scale ( $n_e t$ ), emission measure ( $n_e n_H V$ ). The abundances of O (=N=C), Ne, and Fe (=Ni) of the ejecta were set free and the abundances of Mg, Si, S, and Ar were fixed to the values obtained in the NEI model fit. The best-fit “NEI – Gaussians” model is displayed in Figure 5 and the best-fit parameters are listed in Table 1.

#### 4. DISCUSSION

We compare transmission factors estimated based on the result from the “NEI – Gaussians” model fit with those expected for RS. The transmission factor  $p$  is defined as

$$p = \frac{A - \Delta A}{A}, \quad (1)$$

where  $A$  is the total number of photons emitted by the plasma, and  $\Delta A$  is the number of photons scattered out of our line of sight. We can derive  $p$  for each line from the data, given that the best-fit normalizations of the negative Gaussians and the line intensities of the ISM component correspond to  $\Delta A$  and  $A$ , respectively. The transmission factors derived from the data are listed in Table 2.

Referring to Kaastra & Mewe (1995), we calculate the transmission factors in a case where RS effectively occurs. Under the slab approximation as a simple geometrical model of the SNR rim, Kaastra & Mewe (1995)

**Table 2.** Transitions, centroid wavelengths, and transmission factors of each line.

| Line         | Transition  | Line Centroid (Å) <sup>a</sup> | Transmission Factor <sup>b</sup>       |
|--------------|---|--------------------------------|--|
| Ne IX Heα    | 1s2p <sup>1</sup> P <sub>1</sub> –1s <sup>2</sup> <sup>1</sup> S <sub>0</sub>   | 13.45                          | 0.79 ± 0.11                            |
| Fe XVII Lα   | 2s <sup>2</sup> 2p <sup>5</sup> 3d <sup>1</sup> P <sub>1</sub> –2s <sup>2</sup> 2p <sup>6</sup> <sup>1</sup> S <sub>0</sub> | 15.02                          | 0.70 <sup>+0.04</sup> <sub>–0.08</sub> |
| Fe XVII Lα   | 2s <sup>2</sup> 2p <sup>5</sup> 3d <sup>3</sup> D <sub>1</sub> –2s <sup>2</sup> 2p <sup>6</sup> <sup>1</sup> S <sub>0</sub> | 15.26                          | > 0.85                                 |
| O VIII Lyβ   | 3p <sup>2</sup> P <sub>3/2</sub> –1s <sup>2</sup> S <sub>1/2</sub>  | 16.01                          | > 0.82                                 |
| Fe XVII Lα   | 2s <sup>2</sup> 2p <sup>5</sup> 3s <sup>3</sup> P <sub>1</sub> –2s <sup>2</sup> 2p <sup>6</sup> <sup>1</sup> S <sub>0</sub> | 16.78                          | 0.73 <sup>+0.11</sup> <sub>–0.18</sub> |
| Fe XVII Lα   | 2s <sup>2</sup> 2p <sup>5</sup> 3s <sup>1</sup> P <sub>1</sub> –2s <sup>2</sup> 2p <sup>6</sup> <sup>1</sup> S <sub>0</sub> | 17.05                          | > 0.90                                 |
| O VII Heβ    | 1s3p <sup>1</sup> P <sub>1</sub> –1s <sup>2</sup> <sup>1</sup> S <sub>0</sub>   | 18.63                          | > 0.79                                 |
| O VIII Lyα   | 2p <sup>2</sup> P <sub>3/2</sub> –1s <sup>2</sup> S <sub>1/2</sub>  | 18.97                          | 0.46 <sup>+0.02</sup> <sub>–0.03</sub> |
| O VII Heα(r) | 1s2p <sup>1</sup> P <sub>1</sub> –1s <sup>2</sup> <sup>1</sup> S <sub>0</sub>   | 21.60                          | 0.79 ± 0.08                            |
| O VII Heα(i) | 1s2p <sup>3</sup> P <sub>1</sub> –1s <sup>2</sup> <sup>1</sup> S <sub>0</sub>   | 21.81                          | > 0.76                                 |

<sup>a</sup>Taken from SPEX.<sup>b</sup>Calculated from the best-fit parameters of the “NEI – Gaussians” model.

used a single-scattering treatment where a photon completely escapes from the line of sight at every scattering event. As shown by [Park et al. \(2003\)](#), the ISM plasma of N49 has a particularly bright emission at the southeastern rim. Assuming that the RS occurs dominantly at the southeastern rim, we adopt the same assumption as [Kaastra & Mewe \(1995\)](#). Then, the transmission factor is written as

$$p = \frac{1}{1 + 0.43\tau}, \quad (2)$$

where  $\tau$  is the optical depth of the ISM plasma ([Kastner & Kastner 1990](#)). The optical depth  $\tau$  at the line centroid is given by [Kaastra & Mewe \(1995\)](#) as

$$\tau = \frac{4.24 \times 10^{26} f N_{\text{H}} \left(\frac{n_{\text{i}}}{n_{\text{z}}}\right) \left(\frac{n_{\text{z}}}{n_{\text{H}}}\right) \left(\frac{M}{T_{\text{keV}}}\right)^{1/2}}{E_{\text{eV}} \left(1 + \frac{0.0522 M v_{100}^2}{T_{\text{keV}}}\right)^{1/2}}, \quad (3)$$

where  $f$  is the oscillator strength of the line,  $E_{\text{eV}}$  is the line centroid energy in eV,  $N_{\text{H}}$  is the hydrogen column density in  $\text{cm}^{-2}$ ,  $n_{\text{i}}$  is the number density of the ion,  $n_{\text{z}}$  is the number density of the element,  $M$  is the atomic weight of the ion,  $T_{\text{keV}}$  is the ion temperature in keV, and  $v_{100}$  is the micro-turbulence velocity in units of  $100 \text{ km s}^{-1}$ . We assumed a thermal equilibrium between all ions and electrons and neglected the micro-turbulence velocity. The oscillator strengths and ion fractions for each element were taken from SPEX. In our case, the absorption column density ( $N_{\text{H}}$ ) is the only free parameter.

In [Figure 6](#), we compare the transmission factors estimated from the data and those calculated with equation (2). They are roughly consistent if  $N_{\text{H}}$  is  $(3.0\text{--}10) \times 10^{19} \text{ cm}^{-2}$ , which corresponds to a plasma depth

of  $(10\text{--}34) \times (n_{\text{H}}/\text{cm}^{-3}) \text{ pc}$ . Since the plasma depth is comparable to the diameter of N49,  $\sim 20 \text{ pc}$ , the result supports that RS occurs at the rim of N49. We note that we would underestimate the O abundance by about a factor of 1.8 if we do not take into account the RS effect ([Table 1](#)). This demonstrates the importance of RS in measuring elemental abundances as already pointed out by, e.g., [Kaastra & Mewe \(1995\)](#) and [Miyata et al. \(2008\)](#).

In [Figure 6](#), we found that O VIII Lyα requires a higher column density than the other lines. A possible explanation would be that RS occurs also in the Galactic Halo (GH), as proposed by [Gu et al. \(2016b\)](#). According to [Nakashima et al. \(2018\)](#), GH spectra are represented by a collisional ionization equilibrium (CIE) plasma model with  $kT_{\text{e}} \sim 0.26 \text{ keV}$ . Since such a plasma has a larger optical depth for the O VIII Lyα line than that of the O VII Heα resonance line, the GH should selectively reduce the intensity of O VIII Lyα. We applied the CIE absorption model, *hot* ([de Plaa et al. 2004](#); [Steenbrugge et al. 2005](#)), to the NEI – Gaussians model. The electron temperature and Fe abundance of the *hot* model are fixed to 0.26 keV and 0.56 solar, respectively (the other elemental abundances are fixed to the solar values), by referring to [Nakashima et al. \(2018\)](#). We found that the discrepancy cannot be reduced with the model, where the transmission factors of O VIII Lyα and O VII Heα are calculated to be  $\sim 0.43$  and  $\sim 0.80$ , respectively.

The cause of the observed high O VIII Lyβ/α ratio (the measured value is 0.18 as an upper limit) is not clear. Uncertainties in the model of the Fe-L lines (e.g., [Gu et al. 2019](#)) might partially explain the result since

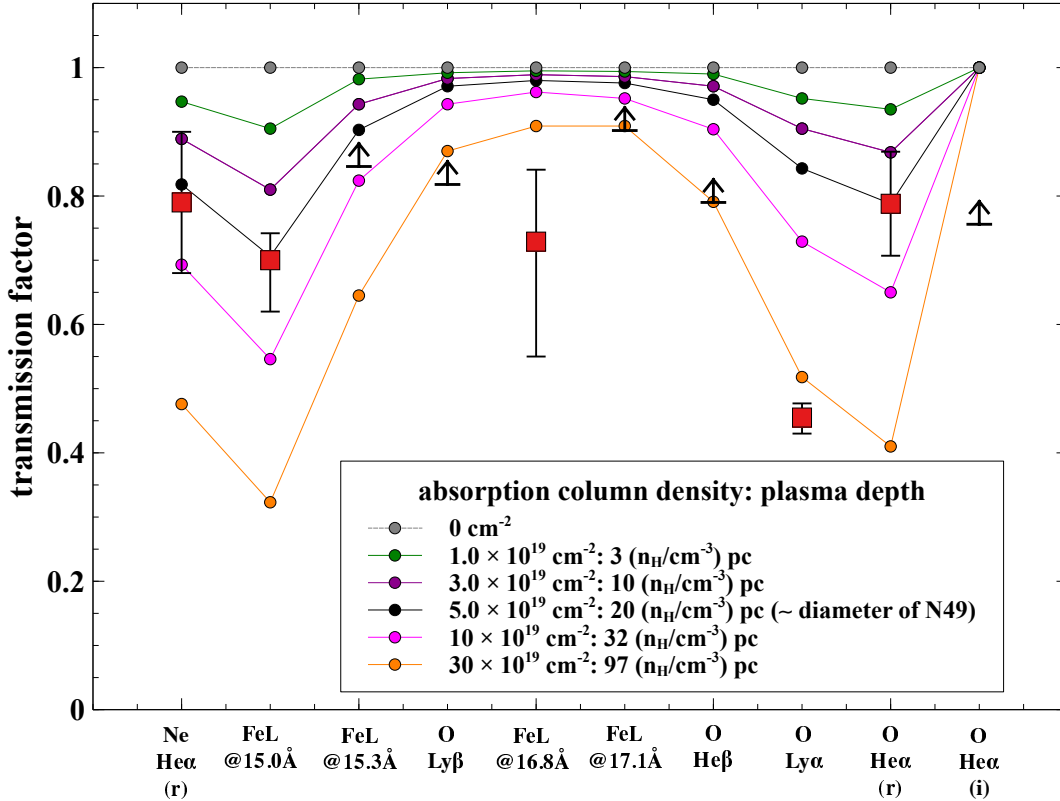


**Figure 6.** Transmission factors for each line. The squares and arrows are the values and lower limits derived from the observational data whereas the circles are those expected for RS. The colors indicate  $N_{\text{H}}$  assumed in the calculation.

O VIII  $\text{Ly}\beta$  overlaps with the Fe XVIII  $\text{L}\alpha$  line. Another possibility to explain the high O VIII  $\text{Ly}\beta/\alpha$  ratio is an effect related to RS. As discussed by [Chevalier et al. \(1980\)](#),  $\text{Ly}\beta$  can be converted to  $\text{H}\alpha$  by a  $3p\text{-}2s$  transition in a collisionless shock through RS. However, this is less plausible because this effect reduces the intensity of  $\text{Ly}\beta$  rather than that of  $\text{Ly}\alpha$ . RS by the ejecta may selectively reduce  $\text{Ly}\alpha$ , which we did not take into account in our analysis. We will be able to evaluate the ejecta contribution by measuring the intensity ratio of the emission lines in Fe  $\text{K}\alpha$ , which originates only from the ejecta (e.g., [Yamaguchi et al. 2014](#); [Uchida et al. 2015](#)). Since Fe  $\text{K}\alpha$  is out of the wavelength band of the RGS, further observations with X-ray microcalorimeters (e.g., [Kelley et al. 2016](#)) is required to clarify this point.

## 5. CONCLUSIONS

We analyzed a high resolution X-ray grating spectrum of LMC SNR N49 obtained with the RGS aboard XMM-Newton. We found that the G-ratio of O VII  $\text{He}\alpha$  is significantly higher than that expected for a thin thermal plasma emission. The ratios of Fe XVII  $\text{L}\alpha$  ( $3s\text{-}2p$ )/( $3d\text{-}2p$ ) and O VIII  $\text{Ly}\beta/\alpha$  also show large residuals from

the model. While an extra CX component well reproduces the G-ratio of the O VII  $\text{He}\alpha$  triplet, the residuals around Fe XVII  $\text{L}\alpha$  and O VIII  $\text{Ly}\alpha$  still remain. On the other hand, RS can fairly reproduce the RGS spectrum. We estimated the optical depth for the RS from the intensities of the scattered lines and found that the depth is roughly consistent with the size of N49. Our results indicate that RS has a particularly strong effect on the measurement of oxygen abundance. As demonstrated by [Hitomi Collaboration \(2018\)](#) with the X-ray microcalorimeter SXS aboard Hitomi ([Kelley et al. 2016](#)), future missions such as the X-Ray Imaging and Spectroscopy Mission (XRISM; [Tashiro et al. 2018](#)) and the Advanced Telescope for High ENergy Astrophysics (Athena; [Nandra et al. 2013](#)) will provide useful means for further studying the effects of RS in SNRs.



## ACKNOWLEDGMENTS

We would like to thank Dr. Hiroya Yamaguchi for fruitful discussions. We also thank Dr. John Raymond for helpful advice. We deeply appreciate all the XMM-Newton team members. This work is supported by JSPS/MEXT Scientific Research grant Nos. JP25109004 (T.T. and T.G.T.), JP19H01936 (T.T.), JP26800102 (H.U.), JP19K03915 (H.U.), and JP15H02090 (T.G.T.).

## REFERENCES

- Banas, K. R., Hughes, J. P., Bronfman, L., et al. 1997, *ApJ*, 480, 607
- Broersen, S., Vink, J., Kaastra, J., et al. 2011, *A&A*, 535, A11
- Cash, W. 1979, *ApJ*, 228, 939
- Chevalier, R. A., Kirshner, R. P., & Raymond, J. C. 1980, *ApJ*, 235, 186
- Cline, T. L., Desai, U. D., Teegarden, B. J., et al. 1982, *ApJL*, 255, L45
- den Herder, J. W., Brinkman, A. C., Kahn, S. M., et al. 2001, *A&A*, 365, L7
- de Plaa, J., Kaastra, J. S., Tamura, T., et al. 2004, *A&A*, 423, 49
- de Plaa, J., Zhuravleva, I., Werner, N., et al. 2012, *A&A*, 539, A34
- Dickey, J. M., & Lockman, F. J. 1990, *ARA&A*, 28, 215
- Gu, L., Kaastra, J., & Raassen, A. J. J. 2016, *A&A*, 588, A52
- Gu, L., Mao, J., Costantini, E., et al. 2016, *A&A*, 594, A78
- Gu, L., Raassen, A. J. J., Mao, J., et al. 2019, *A&A*, 627, A51
- Hitomi Collaboration, Aharonian, F., Akamatsu, H., et al. 2018, *PASJ*, 70, 10
- Jansen, F., Lumb, D., Altieri, B., et al. 2001, *A&A*, 365, L1
- Kaastra, J. S. & Jansen, F. A. 1993, *A&A*, 97, 873
- Kaastra, J. S., & Mewe, R. 1995, *A&A*, 302, L13
- Kaastra, J. S., Mewe, R., & Nieuwenhuijzen, H. 1996, *UV and X-ray Spectroscopy of Astrophysical and Laboratory Plasmas*, 411
- Kaastra, J. S. 2017, *A&A*, 605, A51
- Kastner, S. O., & Kastner, R. E. 1990, *JQSRT*, 44, 275
- Katsuda, S., Tsunemi, H., Mori, K., et al. 2012, *ApJ*, 756, 49
- Kelley, R. L., Akamatsu, H., Azzarello, P., et al. 2016, *Proc. SPIE*, 99050V
- Lodders, K., Palme, H., & Gail, H.-P. 2009, *Landolt Bürnstein*, 4B, 712
- Miyata, E., Masai, K., & Hughes, J. P. 2008, *PASJ*, 60, 521
- Nakashima, S., Inoue, Y., Yamasaki, N., et al. 2018, *ApJ*, 862, 34
- Nandra, K., Barret, D., Barcons, X., et al. 2013, *arXiv e-prints*, arXiv:1306.2307
- Park, S., Burrows, D. N., Garmire, G. P., et al. 2003, *ApJ*, 586, 210
- Park, S., Hughes, J. P., Slane, P. O., et al. 2012, *ApJ*, 748, 117
- Pietrzyński, G., Graczyk, D., Gieren, W., et al. 2013, *Nature*, 495, 76
- Rugge, H. R., & McKenzie, D. L. 1985, *ApJ*, 297, 338
- Russell, S. C., & Dopita, M. A. 1992, *ApJ*, 384, 508
- Sanders, J. S., Fabian, A. C., Allen, S. W., et al. 2004, *MNRAS*, 349, 952
- Schenck, A., Park, S., & Post, S. 2016, *AJ*, 151, 161
- Shigeyama, T. 1998, *ApJ*, 497, 587
- Steenbrugge, K. C., Kaastra, J. S., Crenshaw, D. M., et al. 2005, *A&A*, 434, 569
- Strüder, L., Briel, U., Dennerl, K., et al. 2001, *A&A*, 365, L18
- Tashiro, M., Maejima, H., Toda, K., et al. 2018, *Proc. SPIE*, 1069922
- Turner, M. J. L., Abbey, A., Arnaud, M., et al. 2001, *A&A*, 365, L27
- Uchida, H., Koyama, K., & Yamaguchi, H. 2015, *ApJ*, 808, 77
- Uchida, H., Katsuda, S., Tsunemi, H., et al. 2019, *ApJ*, 871, 234
- van der Heyden, K. J., Bleeker, J. A. M., Kaastra, J. S., et al. 2003, *A&A*, 406, 141
- Waljeski, K., Moses, D., Dere, K. P., et al. 1994, *ApJ*, 429, 909
- Xu, H., Kahn, S. M., Peterson, J. R., et al. 2002, *ApJ*, 579, 600
- Yamaguchi, H., Badenes, C., Petre, R., et al. 2014, *ApJL*, 785, L27

Yamane, Y., Sano, H., van Loon, J. T., et al. 2018, *ApJ*,  
863, 55